

# A Photometric Study of the Supercluster MS0302 with the UH8K CCD Camera: Image Processing and Object Catalogs

N. Kaiser, G. Wilson, G. Luppino, H. Dahle  
Institute for Astronomy, University of Hawaii

## ABSTRACT

We describe in detail the processing of a set of images of the  $z = 0.42$  supercluster MS0302 taken with the UH8K camera at CFHT. The result of this is a pair of seamless combined V- and I-band images of the field, along with a characterization of the noise properties and of the point spread function (PSF), and catalogs of  $\simeq 30,000$  faint galaxies. The analysis involves the following steps: image preparation; detection of stars and registration to find the transformation from detector to sky coordinates; correction for extinction and/or gain variations; modeling of the PSF; generation of images with a circular PSF; image warping and averaging; modeling of the noise auto-correlation function; faint object detection, aperture photometry, and shape measurement. The shear analysis is described elsewhere.

## 1. Introduction

The data described in the paper were taken as part of a program to measure weak gravitational lensing. Reducing these data, taken with the UH8K mosaic camera, has proved to be a complex process. However, after a good deal of experimentation, we feel we have in place a fairly reliable, accurate and largely automated procedure. The purpose of this paper is to describe in detail how the summed images and catalogs of faint objects were constructed, with the weak lensing analysis being described elsewhere (Kaiser et al. 1998). This paper also serves as a technical reference for our group's UH8K 'blank field' survey, which comprises 6 similarly deep fields (Wilson, Kaiser, & Luppino 1999), and which has been analyzed in much the same way. The paper may also possibly be useful for others attempting to reduce data from the UH8K or other similar mosaic cameras, and to this end we highlight some of the inadequacies of our current approach.

The target field, centered roughly on  $\text{RA} = 3^{\text{h}}5^{\text{m}}24^{\text{s}}.0$ ,  $\text{DEC} = 17^{\circ}18'0''.0$ , (J2000) contains three prominent clusters in a supercluster at  $z \simeq 0.42$ . CL0303+1706, was detected optically by Dressler & Gunn (1992), and an Einstein IPC pointed observation revealed the

presence of the two neighboring clusters MS0302+1659 and MS0302+1717 with redshifts  $z = 0.426, 0.425$  (Gioia et al. 1990; citeNPemss91). All three clusters have numerous measured redshifts and form a physically associated complex at  $z \simeq 0.4$ , which fits snugly within the  $0^\circ.5$  square field.

The data were taken at the 3.6m CFHT on the nights 22-24 September, 1995. A total of 17 exposures (11 in I-band, 6 in V-band), each of 900 seconds integration time were obtained. In addition, a number of dark frames and dome flats were taken. Standard stars observations were interspersed between the science exposures, which were performed with small semi-random offsets from the nominal field center (typically  $40''$  offsets) to allow the removal of cosmetic defects and the generation of a seamless contiguous combined image. The image quality was excellent, with stellar FWHM  $\simeq 0''.6$ .

The layout of the paper is as follows: §2: preliminary reduction; §3: detection of stars and registration to find the transformation from detector to sky coordinates; §4: correction for extinction and/or gain variations; §5: modeling of the point spread function (PSF) and generation of images with a circular PSF; §6: image warping and averaging; §7: modeling of the noise auto-correlation function (ACF); §8: faint object detection; §9: aperture photometry and shape measurement.

## 2. Preliminary Reduction

The preliminary reduction of the data was fairly straightforward. We first subtracted from each image a bias, this being a linear ramp fit to the pixel values in the over-scan region. Then for each chip we computed a median of several dark frames and subtracted this from each science image. Then, for each passband and for each chip we computed a median ‘super-flat’ from all the images obtained with that chip, and divided each of the science images by this sky flat. Note that this will have reduced the sensitivity of these images to very extended diffuse flux.

A number of bad columns and other cosmetic defects were clearly visible as high contrast features in the median sky flats. A simple algorithm was used to identify these abnormal pixels and the corresponding pixels in the science images were flagged as unreliable (this is done by setting the pixel value to the ‘magic’ value of -32678 (the most negative number expressible in the 16 bit signed integer pixel format we have used); our image processing software recognizes this value and, generally speaking, the result of any computation involving a magic input value is also set to be magic (the major exception to this rule being the image co-addition).

The science images were then all visually inspected, and a number of further cosmetic defects were flagged as bad data. The data in one of the chips — that in the NW corner — was found to be seriously compromised and these data were discarded.

The images were then cropped from their original, slightly oversized, format to 2048 by 4096 format. The images in the top row (which are read out in the opposite direction to those in the bottom row) were then inverted so that North was approximately aligned with the  $+y$  direction (i.e. the slow readout direction) on all the images.

Finally, we subtracted a smoothed local sky estimate determined from the heights of minima of the images. More specifically, if the locations of the minima are  $x_i$  and have values  $f_i$  then we generated the pair of images  $n(x) = \sum \delta(x - x_i)$  and  $f(x) = \sum f_i \delta(x - x_i)$ , convolved both with a 32 pixel Gaussian to make the smoothed images  $f_s$  and  $n_s$  and then subtracted  $f_s/n_s$ . As with the ‘super-flat’ generation, this will inevitably have suppressed long wavelength features such as possible highly extended diffuse emission from the clusters.

### 3. Astrometric Registration

We now describe how we solved for the mapping from pixel or ‘detector’ coordinates onto a planar projection of the sky.

In the UH8K camera the chips are laid out in two rows each of four 2K by 4K chips laid side by side. There are gaps of about 60 pixels between the sides of the chips and about 20 pixels between the two rows. However, the chips are not precisely laid out on the grid but are slightly rotated and shifted with respect to an ideal tiling grid. In addition to the somewhat irregular chip layout, the CFHT suffers from a field distortion introduced by the telescope wide-field corrector; a pin-cushion distortion with shift amplitude of about 40 pixels, giving a radial shear of  $\gamma \simeq 7.2 \times 10^{-3}$ , at the corners of the roughly 1/2 degree square field.

The registration procedure will impact the weak shear measurement in two ways: First, the telescope distortion, if uncorrected, will mimic the effect of a (negative mass) gravitational lens. This effect is relatively easy to deal with. Secondly, and potentially much more damaging, is the gross anisotropy of the summed image PSF that can result from errors in the registration. Initially we tried to model the distortion assuming a ‘rigid detector’ model, with fixed parameters describing the layout of the rectangular chips in detector plane, but found that this did not yield adequate precision. To obtain sufficient accuracy we found we needed to relax the assumptions of the model; instead we assumed that for each 2K×4K image there is some a low-order polynomial mapping from pixel

coordinates to the rectilinear sky coordinates, but we do not assume that there is any static relationship between the mapping from exposure to exposure — i.e we are assuming that the telescope/detector system can deform in a smooth but otherwise fairly arbitrary manner between exposures. This ‘Jello detector’ model allows for both the telescope distortion and chip layout as well as image deformations associated with filters, atmospheric refraction, thermal expansion and mechanical strain.

### 3.1. Astrometric Reference System

We solved for the parameters of these polynomial mappings — the ‘astrometric solution’ — by minimizing the residuals in the predicted sky positions of a set of reference stars. In principle, given certain conditions on the geometry of the telescope pointings, one should be able to perform an ‘internal’ solution using only the CFHT images and without reference to any external astrometric system (one should then be able to tie this into any other chosen absolute astrometric coordinate system by inspection of the coordinates of any pair of stars). With sufficiently large offsets between exposures, this works quite well, but with the rather small offsets between exposures employed here unfortunately, this turns out to be quite unstable; it is fairly easy to find solutions which map the star positions onto each other to great accuracy, but the solutions tend to have unacceptably large large-scale field distortions. What we did instead was to incorporate the external astrometric information from the start.

The external astrometric data base to which we have chosen to refer our coordinate system is the USNOA catalog (Monet 1998). Unfortunately there are rather few stars which are both present in the USNOA catalog and are non-saturated in the CFH images. This seems to be because to be included in the USNOA catalog an object had to be detected in both red and blue passbands, so many stars which were actually detected in the red drop out of the final catalog. It is also a consequence of the rather long exposure times forced upon us owing to the rather long readout time for the UH8K mosaic; with detectors like the CFH12K the readout time is greatly reduced and this is much less of a problem. To work around this problem we extracted the digitized sky survey (STScI Digitized Sky Survey 1998) red image covering our field and ran our own object detection algorithm which detects most of the USNOA objects, which are predominantly stars, and which were originally derived from the same Palomar plates, as well as a substantial number of stars which did not survive the USNOA selection criteria. In the final astrometric solution we used only fairly bright, but non-saturated, stars from the CFH images, and the overlap with the augmented reference catalog is such that we typically found about 50 stars in common

per 2K×4K CFH image.

The digitized sky survey FITS image contains a ‘world-coordinate system’ definition in the header which relates DSS pixel indices to celestial coordinates (Greisen & Calabretta 1995). After choosing the nominal field center  $(\alpha_0, \delta_0) = (3:5:24.0, 17:18:0.0)$  we then generated the orthographic sky coordinates  $r$  (see below) for each of the DSS stars. Comparing these with the USNOA catalog stars we noticed a small and slowly varying systematic discrepancy between the derived sky coordinates (with amplitude on the order of  $0''.25$ ). We modeled this as a low order polynomial correction

$$r_{\text{USNOA}} = r_{\text{DSS}} + \sum_{l=0}^{l_{\text{max}}} \sum_{m=0}^l a_{lm} f_{lm}(r_{\text{DSS}}) \quad (1)$$

where the mode functions are given by

$$f_{lm}(r) = r_0^{l-m} r_1^m \quad (2)$$

so e.g. for  $l = 2$ , and writing  $r_0 = x$ ,  $r_1 = y$ , the modes are the 3 quadratic functions  $x^2$ ,  $xy$ ,  $y^2$ ; for  $l = 3$ , the modes are the 4 cubic functions  $x^3$ ,  $x^2y$ ,  $xy^2$ ,  $y^3$  and so on. We then applied this correction to the DSS star coordinates, with  $l_{\text{max}} = 3$ , to bring them into agreement with the USNOA system.

The projection we adopted is the ‘orthographic’ projection which is that particular stereographic projection of the sky illustrated in figure 1. This projection is shape (but not size) preserving, which is convenient for weak lensing studies; though had we chosen any of the other standard projections the induced shape distortions would have been on the order of  $\theta^2 \sim 10^{-5}$  and would be negligibly small for the field size here, and similarly, the scale change across the field for the projection we have adopted is on the same order.

To fully define the orthographic projection it is necessary to specify not just the tangent point, but also a rotation angle giving the orientation of the tangent plane. Specifically, this is the rotation of the Cartesian axes  $r_0, r_1$  relative to the longitude and latitude directed unit vectors at the tangent point; this defines the pixel coordinate axes in the final summed images. A natural choice would be to set this so that the ‘ $y$ ’- or  $r_1$ -axis is aligned with a line of longitude, so that, at the field center, North is ‘up’. However, the camera axis was slightly misaligned with North, so with this choice of sky coordinates the bleeding of saturated stars along the slow chip axis would then be slightly tilted with respect to our final coordinate axes which would be awkward later when we come to mask out these features. To avoid this, we adopted a rotation of  $2^\circ.635662$  to approximately align the star trails with the  $r_1$  axis.

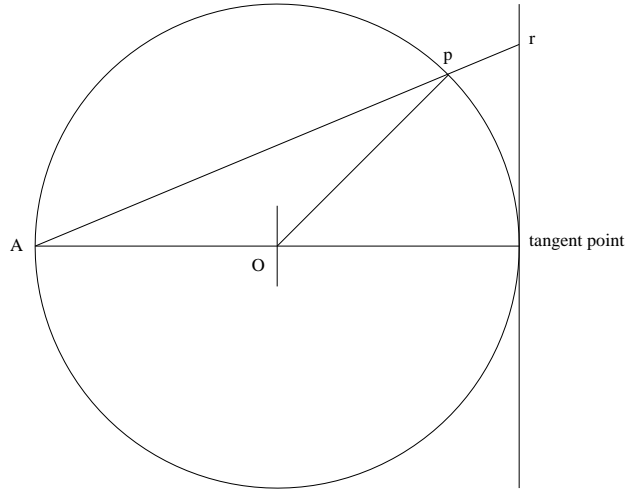


Fig. 1.— Illustration of the orthographic projection we have adopted where we have rotated the coordinate system so that the field center  $(\alpha_0, \delta_0)$ , or tangent point, lies along the  $x$ -axis. A point  $p = (\alpha, \delta)$  on the sky (represented here by the unit sphere) is projected onto the orthographic coordinate plane by projecting the line from the antipode of the tangent point through  $p$  into the tangent plane at point  $r$ . To fully define the  $r$  coordinate system it is necessary to specify the celestial coordinates of the field center  $(\alpha_0, \delta_0)$ , and a rotation angle giving the orientation of the axes of  $r$ -coordinate system relative to the latitude and longitude directed unit vectors at the field center, and a scale factor.

### 3.2. Astrometric Solution

To solve for the image mapping parameters with the MS0302 data we used bright (but non-saturated) stars. Stars brighter than about 20th magnitude are well separated from galaxies in the size-magnitude plane. We typically extracted 100 or so stellar objects per image, or on the order of 1000 stars for a complete mosaic, and of these about one half were reliably measured in the astrometric reference catalog. Stellar centroids were measured to fractional pixel precision using the interpolation scheme described in appendix B. We solved simultaneously for a set of low order spatial polynomials, one per  $2K \times 4K$  image, which map pixel coordinates onto the sky. The solution was obtained by a sequence of refined least squares minimizations. The relatively accurate CCD mosaic star positions ensure that the CFHT images map onto each other with high precision, while the external catalog serves to damp down the kinds of artificial distortion one would otherwise obtain with a purely internal solution.

Specifically, we modeled the mapping from pixel coordinates  $x_{pi}$  (this being the position of the  $p$ 'th star on the  $i$ 'th image) to  $r = r_{\text{USNOA}}$  coordinates as a cubic polynomial just as in (1) with

$$r_p = x_{pi} + \sum_{l=0}^{l=3} \sum_{m=0}^{m=l} a_{ilm} f_{lm}(x_{pi}) + e_{pi} \quad (3)$$

with mode functions as in (2) and where  $e_{pi}$  is the observational error, which we assume to have an isotropic 2-D Gaussian PDF with scale length  $\sigma_{pi}$ , whereas for the reference catalog (the DSS catalog, corrected as described above, and to which we ascribe the index  $i = 0$ )

$$r_p = x_{p0} + e_{p0} \quad (4)$$

or equivalently we can say that (3) applies for all  $i$  with the understanding that  $a_{0lm} = 0$ . This mapping is illustrated in figure 2.

The astrometric solution is that set of star positions  $r_p$  and parameters  $a_{ilm}$  which minimize the sum of the squared residuals:

$$\chi^2 = \sum_p \sum_i e_{pi}^2 / \sigma_{pi}^2 = \sum_p \sum_i (r_p - x_{pi} - \sum_{l,m} a_{ilm} f_{lm}(x_{pi}))^2 / \sigma_{pi}^2 \quad (5)$$

which is quadratic in the parameters  $a_{ilm}$ ,  $r_p$ . For our pointings this yields the well conditioned set of linear equations

$$\partial \chi^2 / \partial a_{ilm} = 0; \quad \partial \chi^2 / \partial r_p = 0 \quad (6)$$

which we solved by LU decomposition for the mode amplitudes  $a_{ilm}$  and star positions  $r_p$ . It is important here to allow for the fact that the DSS coordinates are relatively

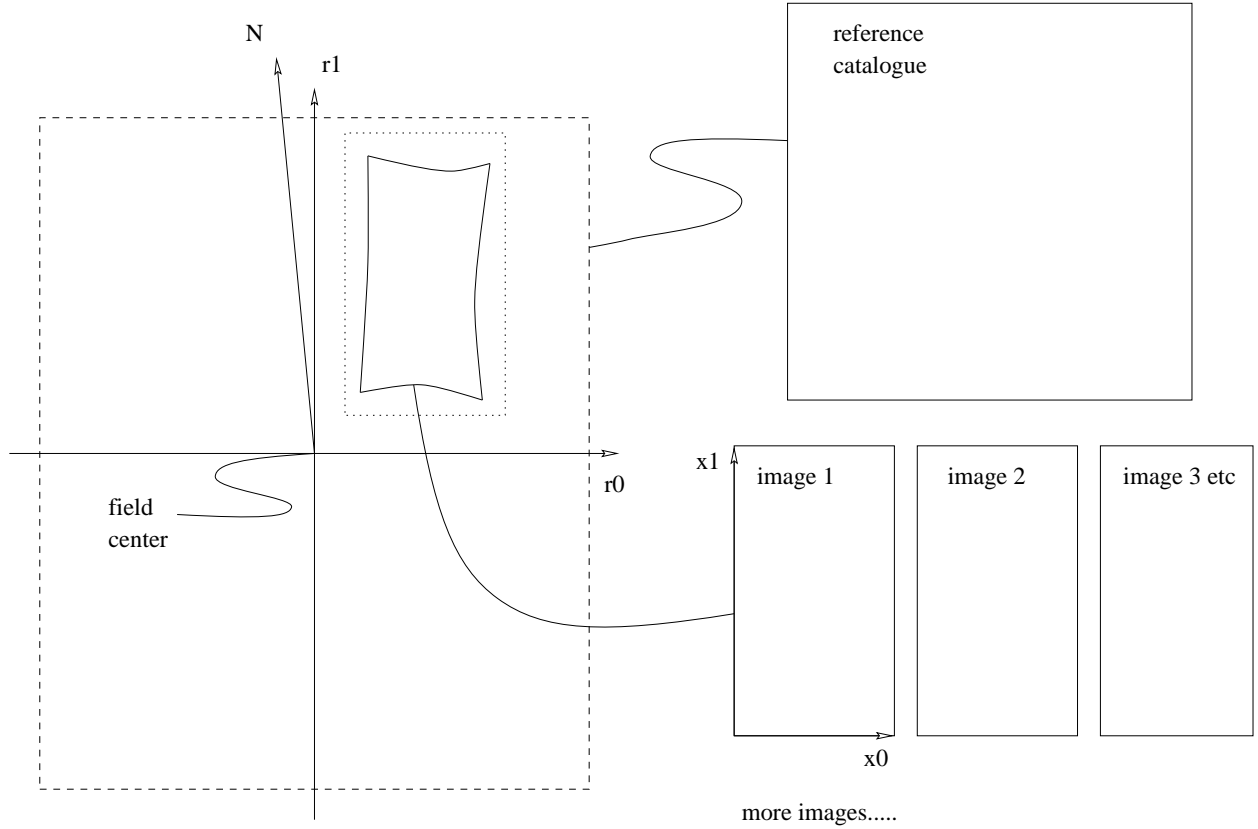


Fig. 2.— Illustration of the mapping from CFHT image pixel coordinates and reference catalog coordinates onto the sky. The orthographic coordinates from the reference catalog map directly onto  $r$ -space with no distortion (but with considerable measurement error). Each of the CFHT science images maps onto the plane in a distorted manner, shown grossly exaggerated in the figure, and which we describe by a low-order spatial polynomial as described in the text. Also shown dotted is the slightly oversize bounding boxes that we compute; these are used when we come to apply the warping to the images to identify which images contribute to a given patch of the sky.



imprecise:  $\sigma_0 \sim 0''.25$  as compared with rms precision for the star centroid coordinates on the CFH images of about  $0''.007$  (see below). Empirically, we found that final variance in the DSS/USNOA coordinates to be very weakly dependent on the brightness of the stars, and, for simplicity, we also assumed the uncertainty in the CFH coordinates to be independent of the stellar flux, but with positional variance smaller than that of the DSS positions by a factor of 200. The precision of our reference star positions should be limited by the systematic error in the USNOA system, so as future, more accurate, astrometric catalogs become available it should be possible to improve our astrometric solution. Our solution corresponds essentially to a maximum likelihood solution under the assumption that the position errors are Gaussian distributed. The resulting set of linear equations is of size  $N_{\text{exposures}} \times N_{\text{chips}} \times N_{\text{modes}} + N_{\text{stars}}$  which, with  $N_{\text{modes}} = 10$  for a cubic fit, is around 2000 and takes on the order of 1 hour to solve on a low end workstation.

The hard work in solving this system of equations is in establishing the labeling of stars by their  $p$ -index, so that we know that two stellar objects in two different images are the same object. To do this we made a sequence of refined approximations for the mapping from pixel  $x$ -space to sky coordinate  $r$  in order to associate objects. In this process we made repeated use of ‘cross-correlation registration’ which, given a pair of catalogs containing a substantial number of objects in common, but with positions given in different coordinate systems, automatically finds a scaling, rotation and translation which maps one coordinate system into the other. The algorithm which accomplishes this is described in appendix A. To get our first approximation to the mapping, accurate to maybe a few arc-seconds at best, we generated approximate detector plane coordinates  $x_e$  for the brightest few hundred objects in each of the exposures by assuming the chips are simply laid out on a regular grid with nominal spacing as described above, and found the scaling, rotation and translation which maps  $x_e$  coordinates to orthographic  $r$  coordinates. Note that ideally this step could have been avoided by using the telescope pointing information encoded in the FITS image headers, but unfortunately some of these turned out to be corrupted. Armed with this first approximation we then extracted, for each image  $i$ , a subset of the reference catalog lying under that image, and then solved for a scaling, rotation and translation for each image mapping pixel coordinate system  $x_i$  onto  $r$  coordinates. This is considerably more accurate than the first solution as we are now approximating the mapping as a set of ‘piecewise undistorted’ patches rather than as a single large undistorted patch. At this stage we also rejected saturated stars from the CFH catalogs and also rejected some corrupted stellar images by selecting on ellipticity.

Using this approximation for the  $r$  coordinates of each object we next accumulated a  $2K \times 2K$  ‘object count’ image covering the entire field in  $r$ -coordinates, and in which the pixel value is the number of star detections. We then slightly smoothed this image, ran our

peak finder to generate a ‘master’ catalog, and to each of the objects assigned a unique identifying index ‘ $p$ ’. We required a minimum of 4 separate detections for an object to be included in this catalog to eliminate spurious detections. We then merged each catalog in turn with this master catalog and thereby inherited the  $p$ -values (by merging a pair of catalogs we mean finding pairs of detections whose positions coincide to within some given tolerance). Finally we concatenated these catalogs, after rejecting extreme outliers, and fed the result to a program which performs the least squares solution of equation (6). This first solution is not perfect, as, due to the approximate initial solution, a small fraction of the stars actually get detected as multiple objects in the master catalog. Armed with our first approximation though, we can generate a refined object count image and corresponding catalog, and then obtain a refined least squares solution for the polynomial coefficients  $a_{ilm}$  and star positions.

As an objective check on how well this procedure worked, we withheld a random subset of 20% of the stars, and did not use these in the registration solution. After solving for the image mapping, we applied the solution to these stars and measured how well their  $r$ -coordinates agreed. Typical results are shown in figure 3. This exercise gave a rms displacement of about  $0''.007$ , or about  $1/30$  of a pixel, for the rms separation (one component) corresponding to a 1-particle rms error of about  $0''.005$ . With this degree of accuracy, any artificial shape distortion due to inaccuracy of the image mapping is, at worst, on the order of  $(\delta\theta/\theta_{\text{obj}})^2$ , where  $\delta\theta$  is typical error in the warping solution and  $\theta_{\text{obj}}$  is the size of the objects, and should be negligible.

The transformation coefficients  $a_{ilm}$  we have thereby obtained give the mapping from  $x_i$ -space (being detector coordinates on the  $i$ th image) to  $r$ -space (i.e. it gives  $r = r(x_i)$  as an explicit function of  $x_i$ ). For actually warping the images what is more useful is the inverse mapping  $x_i = x_i(r)$ , since we need to compute, for each pixel in a target image defined in  $r$ -space, what is the image of the pixel center in  $x_i$ -space, so we need  $x_i$  as an explicit function of  $r$ . (Actually one can perform the image warping using the forward transformation but it turns out to be relatively expensive in terms of computational effort). To obtain the inverse transformation we generated a coarse regular grid of points which span the  $2K \times 4K$  region of  $x_i$ -space occupied by the real pixels, applied the forward transformation to compute the model  $r$ -values and then fed these  $x_i, r$  value pairs to our least-squares program to solve now for the inverse mapping

$$x_i = r + \sum_{l,m} a'_{ilm} f_{lm}(r) \quad (7)$$

to obtain the coefficients  $a'_{ilm}$ . At this point we also set the final pixel scale in orthographic sky coordinates onto which we will map the images. We adopted a pixel scale of  $0''.15$  as

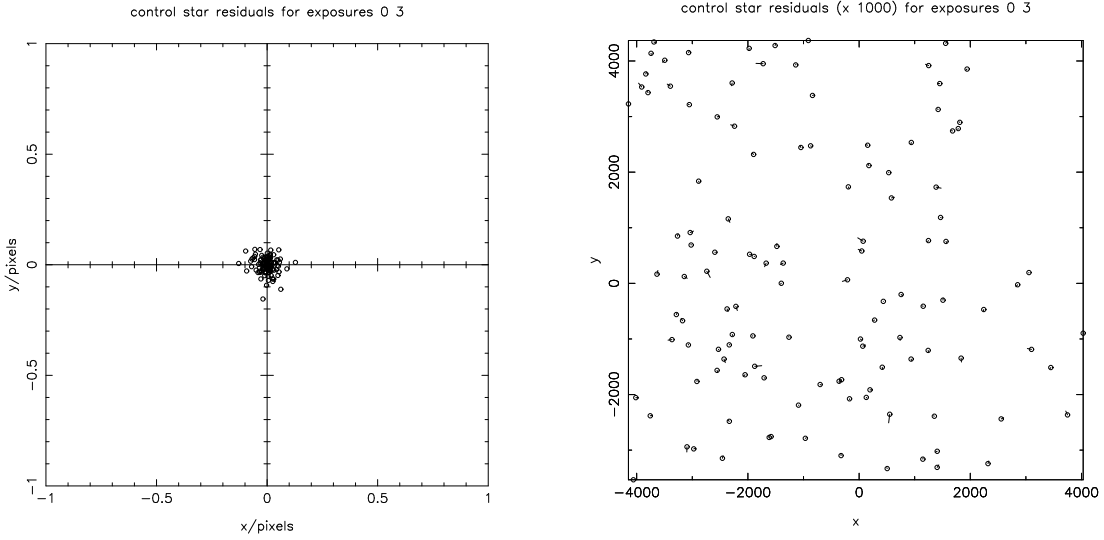


Fig. 3.— Residuals in the image mapping for the control sample. The left hand panel shows the differences between model  $r$ -values for a set of control stars — a randomly chosen subset of 200 stars which were not used in obtaining the astrometric solution — between a typical pair of exposures, in this case the 0th and the 3rd. The unit of length here is the pixel size in the source images or  $0''.207$ . The right hand shows the same residuals, now plotted as vectors with the base of the vector placed at the object position and with the length of the vector exaggerated by a factor 1000. These plots show that the mapping is very accurate. The residual pairwise separation has rms of 7 milliarcsec (per component), corresponding to a 1-particle positional uncertainty (smaller by a factor  $1/\sqrt{2}$ ) of about 5 milliarcsec. The residuals appear to be approximately Gaussian distributed, and we see no obvious systematic variation of the residuals over the image; in particular, we find no tendency for unusually large residuals along the ‘overlap’ regions between the chips.

compared to the original pixel scale of about  $0''.207$ . This is desirable because the original images are quite poorly sampled, the stellar FWHM being  $\simeq 0''.6$  or only about 3 pixels, so aliasing sets in at relatively low spatial frequencies where there is still substantial signal. By interpolating and resampling many images with random offsets we suppress the aliasing to a large degree. The PSF in the final image is then much better sampled, and quantities measured either from stars or galaxies should be less sensitive to pixelization effects. The main disadvantage is that the storage space requirements are roughly doubled.

While the solution we have obtained maps the overlapping images onto each other to impressive precision, the accuracy of the field distortion we have derived leaves quite a lot to be desired. From the coefficients of the polynomial distortion model one can readily compute the distortion tensor  $\phi_{ij} = \partial r_i / \partial x_j$ , the shear  $\gamma_\alpha = \frac{1}{2} M_{\alpha lm} \phi_{lm}$ , and the amplification as a function of position on the final image. Away from the edges of the image these conform quite nicely to the expected circular and approximately quadratic behavior, but close to the edges there are clear signs of errors in the solution. Such errors are to be expected at some level due to the limited density of stars and the relatively large uncertainty in the USNOA positions, and particularly towards the edges of the field. In fact what we see is somewhat larger than what we expect from simulations; this may be due to systematic components to the USNOA positional error, or to stars with anomalous position errors due to proper motions or other effect. This problem is exacerbated by the fact that the chip in the SW corner of the array has a rather large region of cosmetic defects on the side adjoining the rest of the array. This has been masked out, rendering this chip almost disconnected from the rest of the array. For this chip, the errors in the distortion are very large indeed ( $\simeq 1 - 2\%$ , as compared to the expected  $\leq 0.7\%$  shear expected from the telescope itself). This is unfortunate, as it results in an entirely spurious shear in the galaxies which we need to correct for. We describe in §9.2 below how we have dealt with this.

With more recent observations (though of other targets) with the CFH12K camera we have found that this problem can be avoided by taking a sequence of preliminary short 2 minute exposures with large offsets (roughly half the chip dimensions) and using these to obtain the astrometric solution. From these short images one can generate a reference catalog to which one can register the longer science exposures, these being taken with relatively small offsets. The solution obtained from the astrometric fields still suffers from errors at the very edge, but these lie beyond the edge of the region covered by the science exposures and therefore have little impact on the final analysis. A further advantage of the shorter exposures is a greater overlap between non-saturated CFHT observed stars and stars in the USNOA catalog. This further improves the quality of the astrometric solution, and obviates the need for augmenting the USNOA catalog with DSS stars.

#### 4. Correction for Extinction and Gain Variations

Using the catalogs of reference stars described in the previous section we solved, again in a least squares manner, for a set of magnitude offsets (one set for the chips and one set for the exposures) which account for any variation in sensitivity between chips (and imprecision in the zero-points determined from standard stars) and for varying extinction between exposures. These multiplicative corrections were very small; typically  $\sim 0.01$  magnitudes with maximum correction of  $\simeq 0.04$  magnitudes, so we can conclude that the observing conditions were accurately photometric.

#### 5. Modeling the PSF

The seeing in these images is very good, ( $\text{FWHM} \simeq 0''.6$ ) which means that departures from the pure circular PSF expected from atmospheric turbulence become very noticeable. These departures from circularity in the PSF, which we shall denote by  $g(x)$ , most likely stem from several sources, but principally from guiding errors and aberrations of the telescope optics. In the latter category there is a well known astigmatism, thought to be caused by an imperfection in the primary mirror figure. This is readily seen as a variation in the PSF ellipticity as the camera is moved up and down through focus. Consequently, this effect couples to any tilting of the chips relative to the focal plane. The result of this is a PSF which varies smoothly across any one chip, but which jumps discontinuously as one passes to a neighboring chip.

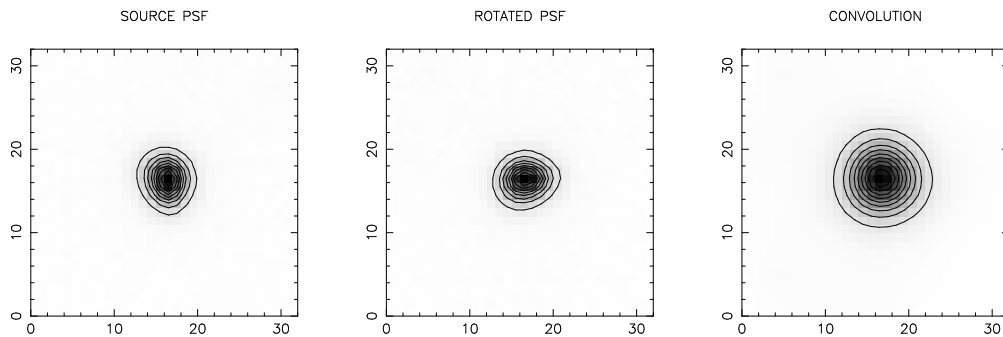


Fig. 4.— Example PSFs. The left hand panel shows a typical PSF. It is a realization of a 1st order polynomial fit to the stars in the final image patch lying in the SE corner of the field. The middle panel shows the same PSF but rotated through 90 degrees and the right hand panel shows the convolution of the two.

This is a considerable nuisance for weak lensing studies where one needs to accurately

model and correct shapes of faint galaxies for variations in the PSF. In dealing with single chip cameras one can model the PSF as a smooth low-order polynomial. This is clearly inappropriate here since the PSF variation in the summed images will have step-like discontinuities. This is much harder to model accurately. Another problem, though one which is not restricted to mosaic cameras, is that great care must be taken in averaging of images if stars in the final image are to be used to monitor the PSF; the problem is that statistically robust averages like the median will tend to ignore unusually distorted stellar images, while the image of a faint galaxy on the same image will not be down-weighted. The approach we have adopted here is to re-convolve each of the source images with a kernel  $g^\dagger = R_{\pi/2}(g)$ , a 90 degree rotated version of the PSF, in order to render the final PSF approximately quadrupole free. Figure 4 shows a typical PSF and the result of convolving it with a 90° rotated version. Note that this reconvolution does not involve any actual loss of information since it is applied after the photon counting noise fluctuations have been realized in the measurement process.

For each source image we selected a sample of  $\sim 100$  stars and extracted a set of ‘postage stamp’ images centered on the star and 32 pixels on a side. To remove stars which were corrupted by cosmic rays etc we computed a median of the stellar images, and for each star computed the mean and maximum deviation from the median, and rejected those with abnormally large deviations. We then solved, by unweighted least squares, for a model in which  $g(x; x_0)$ , this being the shape of a star lying at  $x_0$  on the chip, is a low order polynomial

$$g(x; x_0) = \sum_{l,m} g_{lm}(x) f_{lm}(x_0) \quad (8)$$

with mode functions  $f_{lm}$  just as in equation (2), but now with image valued coefficients  $g_{lm}(x)$ . We used a 1st order model, which seemed to adequately describe the PSF variations we see. For each source image we then generated a ‘re-circularized’ image:

$$f_{\text{recirc}}(x_0) = \sum_{l,m} f_{lm}(x_0) (R_{\pi/2}(g_{lm}) \otimes f)_{x_0} \quad (9)$$

Using a 90-degree rotation is only an approximate method for re-circularizing, but in this case works quite well, and gives re-convolved images with PSF with quadrupole anisotropy of  $\lesssim 1\%$ , which is a great improvement over the grossly anisotropic initial PSF. Note that further low-level anisotropy in the PSF in the summed images will result from the image warping. We describe in §9 below how we have corrected for these effects.

## 6. Image Warping and Averaging

Armed with the results of the previous sections: the files containing the parameters  $a'_{ilm}$  of the mapping from sky coordinates  $r$  to chip coordinates  $x$  and the table of extinction/gain corrections, we next generated a pair of averaged images — a raw and a re-circularized version. As the final image spans  $\sim 12,000$  pixels at our chosen  $0''.15$  pixel scale, rather than generate a single image we chose to generate a  $6 \times 6$  grid of slightly overlapping square patches each of size  $2048 \times 2048$  pixels, the central  $2000 \times 2000$  sub-images of which form a contiguous tiling of the sky.

More specifically, for each patch of the grid and for each exposure, we inspected a set of ‘bounding box’ files generated in the registration process to determine which source images contribute to that patch, and generated a stack of  $2048 \times 2048$  images, one per exposure, by applying the polynomial warping transformations and also multiplicative corrections for extinction etc. The warping was done with bi-linear interpolation as described in appendix B. The stack of images was then combined simply by taking the median. The median is strictly less than optimal — the final variance is theoretically larger than a simple averaging (assuming a large number of equally noisy source images) by a factor  $\pi/2$  (Kendall & Stuart 1977) — but it is extremely robust to non-Gaussian noise such as cosmic rays. Moreover, we have found that in practice the final variance is barely larger than that obtained from more sophisticated methods involving rejection of outliers and then averaging with weights proportional to  $1/\sigma_{\text{sky}}^2$ , presumably because of low-level systematic errors in the sky subtraction that start to become apparent when one averages large numbers of images. It should be mentioned that in these data there were only relatively minor fluctuations in the seeing from image to image, and it may well be that the simple median averaging approach would not work well when combining more heterogeneous data. Also, a somewhat more sophisticated approach has been used to combine the images in our UH8K blank field survey (Wilson, Kaiser, & Luppino 1999).

The photometric scale of these final images is such that a single count in the averaged images corresponds to a magnitude of  $I = 32.39$ ,  $V = 32.49$ . For our blank field observations we also computed an estimated inverse sky variance as the sum of the inverse variance of the contributing images, as described below, and stored  $\sigma_{\text{sky}}$  in an auxiliary image, but for MS0302 this was not done.

### 6.1. Astrometric Information

The astrometric information which describes the mapping from pixel indices in the averaged images is stored in the FITS header for each image patch using the convention of Greisen & Calabretta 1995. This ‘world coordinate system’ is automatically decoded by later versions of ‘saoimage’ and ‘ximtool’ so that the cursor position read-out fields display  $(\alpha, \delta)$  rather than pixels.

The claimed precision of the USNOA catalog is on the order of  $0''.25$ , and so it is reasonable to assume that the final uncertainty in our coordinates (which depends mainly on the systematic component of the USNOA astrometry errors) is no larger than this. Small-scale random errors in our solution should be much smaller than the systematic errors, and our coordinates should be quite adequate for e.g. the purpose of making slit masks for multi-slit spectroscopy.

### 6.2. Masking

The saturated bright stars suffer from bleeding, reflection, and diffraction spikes. These confuse the faint object detection algorithm. To remove the resulting spurious detections we have manually generated a set of mask files, one for each patch of the quilt of the images, containing rectangles which enclose these trails and other obviously suspect parts of the final averaged images.

To do this we ran our object finding algorithm with a low significance threshold. Displaying these objects superposed on the average image proved to be a very effective way of identifying these trails since even very faint trails showed up as conspicuous streaks of false detections and we were thereby able to interactively generate the mask.

## 7. Noise Properties and Limiting Magnitude

These images are sky noise dominated; the number of photons being counted being a Poisson distributed random variate with mean proportional to the intensity, or, for the high counts we have here, Gaussian distributed to a very good approximation. The faint galaxies are typically well below sky, so the contribution to the noise associated with the background galaxy signal is negligible and we can safely model the sky noise in any source image as effectively flat and homogeneous.

We estimated the rms sky noise fluctuation  $\sigma_{\text{sky}}$  in the averaged images by measuring



the curvature of the pixel value distribution around the mode, as this is not greatly affected by the skewing of the distribution by the signal. There will be some spatial variation in the sky variance due to the somewhat reduced integration in the regions near the chip boundaries, but for simplicity these have been ignored here.

The noise in the averaged images has short range correlations from the mapping, interpolation and re-sampling. We have modeled the noise auto-correlation function using a simple simulation in which incoherent white-noise images were generated, interpolated and resampled just as for the real images. Specifically, we dithered these images on a  $4 \times 4$  grid of spacing 0.25 source pixels. This is not identical to the real data, where the offsets were effectively randomly scattered over the unit square, but as we have a reasonably large number of images this simple model should fairly accurately mimic the real noise correlations. These images were then auto-correlated to obtain a small FITS image of the noise ACF. The ACF of the noise in the re-circularized images can also then be obtained simply by convolving this twice with the rotated PSF.

It is conventional to quote the limiting sensitivity as the rms sky fluctuation expressed as a ‘magnitude per square arc-second’, this being the rms fluctuation per pixel if re-binned to  $1''$  pixels and expressed as a magnitude. Allowing for the noise correlations we find that in the well covered regions in these summed images this is  $I = 28.1$ ,  $V = 28.7$ .

## 8. Faint Object Detection

The faint object detection algorithm we have used is essentially as described in Kaiser, Squires, & Broadhurst (1995), in that we smooth the images with a sequence of ‘Mexican hat’ filters of progressively larger size, track the peak trajectories, and define an object to be the peak of the significance (being the height of the peak divided by the rms fluctuation for that smoothing scale) along the trajectory. The program which accomplishes this task is called `hfindpeaks`. The only major modification we have made is to allow for the correlation of the noise in the images due to the interpolation and re-binning. This is done by having `hfindpeaks` read a small  $32 \times 32$  pixel image of the noise ACF, generated as described in 7, and then properly compute the sky variance for each smoothing scale.

More specifically, we used a filter which is a normalized Gaussian ball of scale  $r_g$  minus another normalized concentric Gaussian of scale  $2r_g$ . The filter scale was varied from 0.5 to 20.0 with equally spaced logarithmic intervals  $\Delta r_g = 0.2r_g$ . The algorithm was run on the raw (i.e. not re-circularized) images, and all objects with significance  $\nu > 4$  were output (though in the weak lensing analysis more conservative cuts were made). The output of the

program is a `lc` format catalog (see appendix C) containing the items listed in table 1.

Table 1: `hfindpeaks` output

name	type	description
<code>x</code>	2-vector	peak location $x_i$
<code>lg</code>	scalar	approximate flux $l_g$
<code>rg</code>	scalar	Gaussian detection scale ( $\times 0.66$ ) $r_g$
<code>eg</code>	2-vector	smoothed peak ellipticity $e_\alpha^g$
<code>fs</code>	scalar	smoothed peak height $f_s$
<code>nu</code>	scalar	significance $\nu$

The quantity  $l_g$  is a rather crude estimate of the flux obtained assuming a Gaussian profile for the object in question, and the scaling of the detection radius is also based on a Gaussian shape. The peak ellipticity  $e_\alpha^g$  is computed from the second derivatives of the smoothed image at the peak location as  $e_\alpha^g = M_{\alpha lm} \partial_l \partial_m f / \partial_n \partial_n f$ . The significance  $\nu$  is the value of the smoothed field peak divided by the rms of the noise fluctuations when smoothed at the same scale.

## 9. Faint Object Photometry

### 9.1. Aperture Photometry

The catalog generated by `hfindpeaks` was then processed by the command `apphot` which performs basic aperture photometry. The size of the aperture was set to be 3 times the Gaussian detection scale  $r_g$  and from the pixels within this radius we computed the quantities listed in table 2.

### 9.2. Shape Measurement

Following processing with `apphot` we processed the catalog with the command `getshapes3` to obtain the weighted second moments and other quantities that are used for weak shear analysis as described in (Kaiser 1999). This added to the catalog the entries listed in table 3.

The windowed flux is defined in the continuum limit as

$$F = \int d^2r w(r) f_s \quad (10)$$

Table 2: `apphot` output

name	type	description
<code>flux</code>	scalar	sum of pixel values
<code>mag</code>	scalar	magnitude
<code>rh</code>	scalar	half light radius $r_h$
<code>rp</code>	scalar	Petrosian radius $r_p$
<code>rql</code>	scalar	radius containing 25% of the light
<code>nqu</code>	scalar	radius containing 75% of the light
<code>nbad</code>	scalar	number of bad pixels
<code>fmax</code>	scalar	value of hottest pixel $f_{\max}$

Table 3: `getshapes3` output

name	type	description
<code>F</code>	scalar	windowed flux $F$
<code>q0</code>	scalar	size $q'_0$
<code>q</code>	2-vector	polarization $q'_\alpha$
<code>P0</code>	2-vector	size response $P'_0$
<code>P</code>	2x2 matrix	polarization response $P'_{\alpha\beta}$
<code>R</code>	2-vector	windowed flux response $R'_\alpha$
<code>Z</code>	2x2 matrix	fourth moment $Z'_{\alpha\beta}$

where  $f_s$  is the re-convolved image, and is approximated as a simple sum over pixels with no attempt at sub-pixel precision. The window function  $w(r)$  was taken to be a Gaussian with scale  $\sigma$ :  $w(r) = \exp(-r^2/2\sigma^2)$ . The second moments

$$q_A = (q_0, q_\alpha) = \frac{1}{2} M_{Alm} \int d^2r w(r) r_l r_m f_s \quad (11)$$

are similarly approximated, but the quantity actually output is rescaled by dividing by the windowed flux:  $q'_A = q_A/F$ , so that the moments  $q'_A$  have dimension of (pixels)<sup>2</sup>. The quantities  $P_{A\beta}$ ,  $R_\alpha$  are computed from the unreconvolved image using a similarly discretized version of equation (48) of (Kaiser 1999), and again the primes indicate that these are also output after normalization by  $F$ .

The computed polarization values  $q'_\alpha$  here suffer from two instrumental biases: residual anisotropy of the PSF and PSF distortion introduced in applying the image mapping. We now describe how we corrected for these.

### 9.2.1. Correction for PSF Distortion from Image Mapping

The problem here arose because, for simplicity, we applied the recircularization process in detector coordinates, so the image warping will have sheared the PSF and thus will necessarily have affected the shapes of small objects. This problem was exacerbated by the substantial systematic error in our astrometric solution. Had we instead contrived to generate a re-convolved PSF  $g^\dagger \otimes g$  that was slightly anti-sheared so as to make the final PSF in the orthographic sky projection circular, this problem would have been avoided and the (Kaiser 1999) analysis could then be applied. Alternatively, had we not taken out the telescope distortion (nor added further erroneous distortion) but measured the shapes in detector space then again, the (Kaiser 1999) analysis could again be directly applied to generate a set of shear estimates  $\hat{\gamma}_\alpha$ , but with the understanding that these would in the final analysis need to be corrected for the telescope distortion. The latter presents no particular problem since the telescope distortion is quite accurately measured from our CFH12K astrometry observations on other fields.

The transformation from detector coordinates to orthographic sky coordinates is simply a shear applied after all convolutions, so its effect on the moments  $q_\alpha$  can be easily computed using the precepts of Kaiser, Squires, & Broadhurst (1995). That work considered the response of the ellipticity  $e_\alpha \equiv q_\alpha/q_0$  to a shear. Here we have instead moments normalized by the flux:  $q'_\alpha = q_\alpha/F$ , but using the same line of reasoning, and specializing to the case of a Gaussian window function, one finds that applying the shear

operator  $f \rightarrow f' \simeq f - \gamma_\alpha M_{\alpha ij} r_i \partial_j f$  gives a ‘post-seeing shear response’ of

$$\Delta q'_\alpha = \gamma_\beta \left[ 2q'_0 \delta_{\alpha\beta} - Z'_{\alpha\beta}/2\sigma^2 + 2q'_\alpha q'_\beta/\sigma^2 \right] \quad (12)$$

where

$$Z_{\alpha\beta} \equiv M_{\alpha ij} M_{\beta lm} \int d^2r w(r) r_i r_j r_l r_m f_s \quad (13)$$

and  $Z'_{\alpha\beta} = Z_{\alpha\beta}/F$ . To apply this we generated an image of the shear from the image mapping polynomial coefficients, and the  $q'_\alpha$  values were corrected by subtracting (12). One should really correct the last term here in (12), which being quadratic has a non zero noise induced expectation value, but for simplicity, this rather small extra correction was ignored.

### 9.2.2. Correction from Residual PSF Anisotropy

Re-convolving with a  $90^\circ$  rotated PSF is only an approximate re-circularizer. The residual anisotropy was on the order of 1 percent, and so can be important for small galaxies. We also found that low level PSF anisotropy over and above that expected was introduced in the image mapping. To correct for these residual effects we have applied essentially the KSB approximation: i.e. we have assumed that the residual anisotropy can be modeled as a convolution of a circular PSF with a kernel  $k(r)$  which is compact as compared to the overall width of the PSF. Under this assumption, applying the ‘smear operator’  $f \rightarrow f' \simeq f + \frac{1}{2} p_{lm} \partial_l \partial_m f$ , where  $p_{lm} \equiv \int d^2r r_l r_m k$  is the unweighted second moment of the kernel, gives a response

$$\Delta q'_\alpha = \frac{p_\beta}{\sigma^2} \left[ (\sigma^2 - 2q'_0) \delta_{\alpha\beta} + Z'_{\alpha\beta}/4\sigma^2 - q'_\alpha q'_\beta/\sigma^2 \right] \quad (14)$$

where  $p_\alpha \equiv \frac{1}{2} M_{\alpha lm} p_{lm}$ .

To apply this correction we used (14) to infer the  $p_\beta$  values for a set of stars and fit these as a 4th order spatial polynomial, and then corrected each galaxy moment  $q'_\alpha$  accordingly.

## 10. Conclusions

In this paper we have tried to describe in some detail the techniques we have developed for processing of images taken with mosaic CCD cameras such as the UH8K and the CFH12K. These techniques have evolved continuously over several years now, and are surely not yet optimal in many regards, but some aspects of the analysis seem to work quite well.

We hope the description here may be helpful either to people who wish to use our final images and object catalogues — which we hope to make available electronically — or to people who wish to use our ‘imcat’ software, which again is available on the internet.

It is a pleasure to acknowledge helpful conversations, encouragement and also detailed comments on a draft of this paper from Yannick Mellier, Thomas Erben, and Emmanuel Bertin.

## REFERENCES

- Dressler, A., & Gunn, J. E. 1992, ApJS, 78, 1
- Gioia, I. M., Maccacaro, T., Schild, R. E., Wolter, A., Stocke, J. T., Morris, S. L., & Henry, J. P. 1990, ApJS, 72, 567
- Greisen, E. W., & Calabretta, M. 1995, ASP Conf. Ser. 77: Astronomical Data Analysis Software and Systems IV, 4, 233
- Kaiser, N. 1999, submitted to ApJ
- Kaiser, N., Squires, G., & Broadhurst, T. 1995, ApJ, 449, 460,
- Kaiser, N., Wilson, G., Luppino, G., Kofman, L., Gioia, I., Metzger, M., & Dahle, H. 1998, ApJsubmitted, <http://xxx.lanl.gov/abs/astro-ph/9809268>
- Kendall, M., & Stuart, A. 1977, The advanced theory of statistics. Vol.1: Distribution theory (London: Griffin, 1977, 4th ed.)
- Monet, D. 1998, <http://archive.eso.org/skycat/servers/usnoa>
- Stocke, J. T., Morris, S. L., Gioia, I. M., Maccacaro, T., Schild, R., Wolter, A., Fleming, T. A., & Henry, J. P. 1991, ApJS, 76, 813
- STScI Digitized Sky Survey. 1998, <http://stdatu.stsci.edu/dss>
- Wilson, G., Kaiser, N., & Luppino, G. 1999, in preparation

### A. Cross-correlation Registration

The registration process described in §3 is essentially automatic, though there is some human intervention in the outlier rejection and refinement of the astrometric solution. An essential ingredient is the algorithm for approximately registering a pair of catalogs. The algorithm only seeks to find a scaling, rotation and displacement that effects the transformation from one coordinate system to the other. While crude, this may at least allow one to merge or match the catalogs — i.e. find pairs whose coordinates agree to some small tolerance — and once the correspondence between objects in the different catalogs is established one can readily solve for more elaborate transformation models (such as the low order spatial polynomial models used extensively here).

The problem is illustrated in the figure 5. The solution we use is conceptually very simple; if for each catalog we make a larger catalog containing all pairs of objects from the source catalog, and then plot these pairs in  $\phi, \log(d)$  space (where  $\phi$  is the orientation angle of the pair and  $\log d$  is the natural logarithm of the pair separation) then the two pair catalogs should just be shifted with respect to each other, with the shift in  $\phi$  simply being the rotation between the two coordinate systems, and the shift in  $\log d$  being the logarithm of the scale factor.

These rotation and scale factors can readily be determined by autocorrelation using the FFT. We simply generate a pair of images of the counts of pairs in  $(\phi, \log d)$  space and compute their cross-correlation, which shows a strong peak at the location of the real shift. Once we have the scale and rotation, we can apply these to the first catalog. This should now simply be a laterally shifted version of the second catalog, and we can solve for the shift by again making and cross-correlating a pair of images of the counts of the objects.

Even if the input catalogs satisfy the scale, rotation and translation transformation exactly, the result of `acfregister` will be somewhat imprecise due to the finite pixel size in the images used here. Typically we use images of size  $512 \times 512$  pixels, though the peak is located to fractional pixel precision, typically  $1/30$  pixel or thereabouts, giving a fractional precision in angle of  $\sim 10^{-4}$ . The range of  $\log d$  can be quite large, and if the image size were set to encompass the whole range of  $\log d$  then there would be loss of precision. To avoid this problem we have wrapped the  $\log(d)$  coordinate with a range of unity, so the precision in  $\log(d)$  is of the same order as the angle.

This algorithm works quite well with real data, provided there is a reasonable overlap between the objects in the two input catalogs, and will still usually generate an acceptable solution even if a substantial fraction of the objects in one catalog are missing in the other. We have found that the algorithm can become confused with certain pairs of input catalogs

— because of the periodic boundary conditions implied by the use of the FFT, it can, for instance, give a solution which is an alias of the desired solution (with the shift incorrect by the side of the box say), but provided the catalogs roughly cover the same area this is not a problem.

## B. Two-Dimensional Interpolation

Here we describe our sub-pixel interpolation scheme. We used interpolation at two points in the process: first when we determined the centroids of stars and second when we warped the images. The interpolation schemes for these two steps are different.

The object detection algorithm we used for detecting stars for registration is very simple; we smoothed the image  $f$  with a Gaussian smoothing kernel with size similar to the psf and then located the local maxima of the smoothed flux  $F$  to obtain a integer pixel position  $(i_x, i_y)$ . To refine this we computed first derivatives

$$\begin{aligned} F_x &= (F_{i_x+1, i_y} - F_{i_x-1, i_y})/2 \\ F_y &= (F_{i_x, i_y+1} - F_{i_x, i_y-1})/2 \end{aligned} \tag{B1}$$

and second derivatives

$$\begin{aligned} F_{xx} &= F_{i_x+1, i_y} - 2F_{i_x, i_y} + F_{i_x-1, i_y} \\ F_{yy} &= F_{i_x, i_y+1} - 2F_{i_x, i_y} + F_{i_x, i_y-1} \end{aligned} \tag{B2}$$

and then computed refined positions according to

$$\begin{aligned} x &= i_x - F_x/F_{xx} \\ y &= i_y - F_y/F_{yy} \end{aligned} \tag{B3}$$

Our pixel coordinate labeling convention differs from the FITS standard in which pixel centers have integer values with FORTRAN style unit offset indexing — so the physical region covered by a  $N \times N$  chip is defined to be  $0.5 < x, y < N + 0.5$ . Here our pixel centers have half-integer values and we use the ‘c’-style zero offset indexing so we have  $0 < x, y < N$ , and the center of the corner pixel, for instance, is  $(x, y) = (0.5, 0.5)$ .

When we warped the images we used a different type of interpolation. The pixel values are samples of a continuous function  $f$  (being the convolution of the sky flux with the box-like pixel response function) on a grid points  $(i_x + 1/2, i_y + 1/2)$ . A point  $(x, y)$  lies within a square defined by four of these samples. To interpolate the  $f$  value we added a fifth sample at the center of the square which is the average of the four corner values. Joining the four corners to the center divides the square into four triangles, with the interpolation point lying in one of these. We took as our estimate of  $f(x, y)$  the height at  $(x, y)$  of the plane which passes through the three samples at the corners of this triangle. The interpolated  $f$



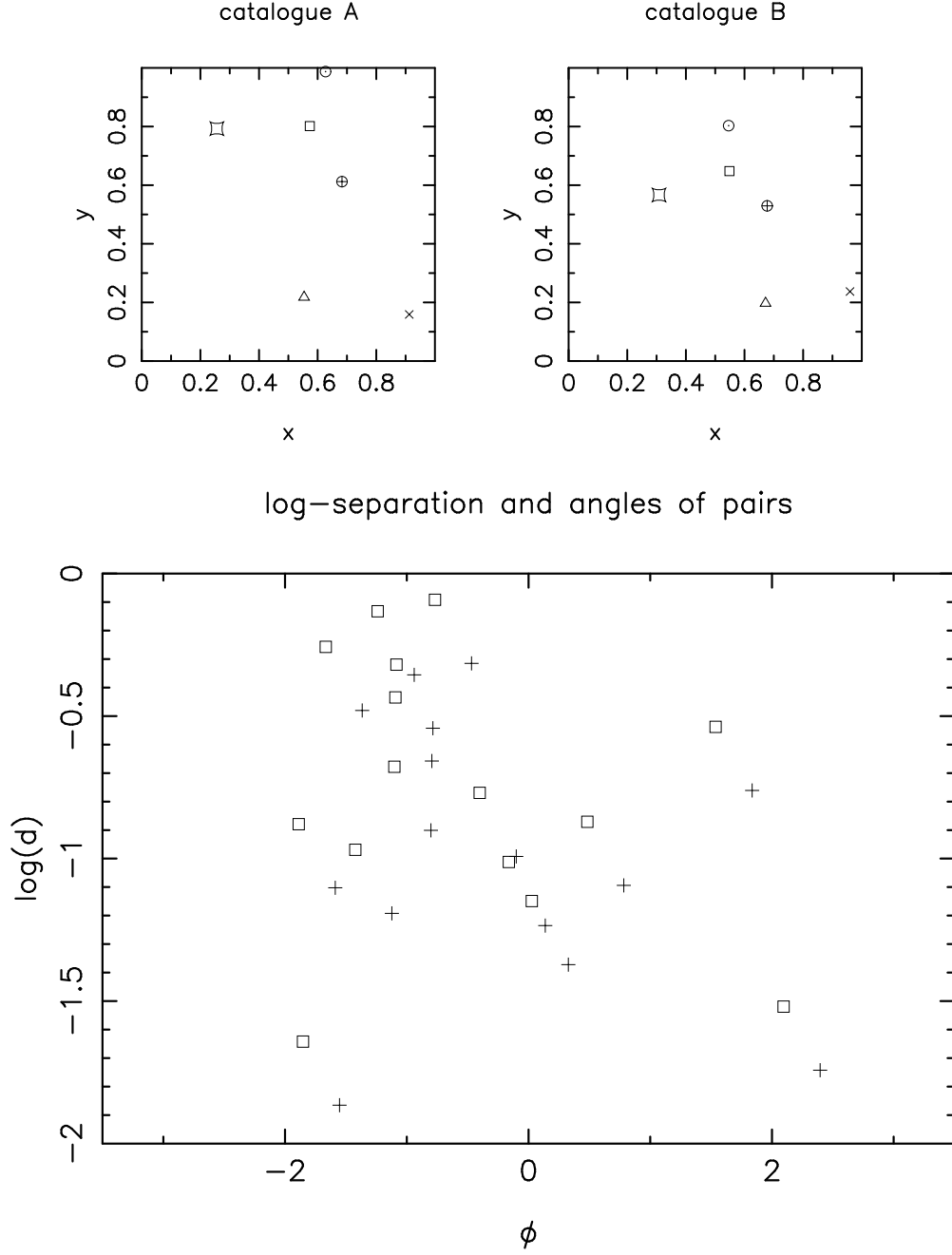


Fig. 5.— Upper panels show the same set of 6 objects, but with coordinates in catalog-B being scaled (by a factor 0.8), rotated (by 0.3 radians) and shifted (by  $(0.3, -0.1)$ ) with respect to catalog-A. Lower panel shows a plot of pairs from the each of the catalogs in orientation *vs* log separation space (with the pairs from catalog-B shaded). It can easily be shown, and is readily apparent from the figure, that the pairs are simply shifted with respect to each other.

values thus obtained are continuous, but have discontinuity of gradient along the vertical, horizontal and diagonal lines connecting the original sample grid.

### C. Catalog Format

Along with the summed images, our database, which we plan to make available electronically, also contains catalogs of objects and numerous auxiliary tabular information. The format of these catalogs and other tables is defined by the program ‘`lc`’ (for list catalog) which, as its name implies, in its default mode, simply generates an ASCII format listing of a catalog. However, with its numerous command line options, `lc` becomes a fairly versatile filter for manipulating catalogs.

The `lc` program is very similar to the UNIX command `awk`, in that it processes catalogs one object at a time; reading an object from standard input - performing some manipulation on the contents of the object as specified by instructions supplied on the command line - and writing the result to standard output, but with the following distinctions: a) fields or entries in the object are referred to by symbolic names rather than by column number; b) entries may be scalars, vectors or matrices of arbitrary rank (there is also some limited support for textual entries) and c) `lc` can read and write in binary format, resulting in a large gain in efficiency.

Operations to be performed are specified as command line strings in a simple ‘reverse-Polish’ notation. All of the standard `c` math library functions and operators as well as a number of specialized functions and operators (such as vector products, matrix inversion etc.) are supported.

Our photometry packages are implemented as ‘filters’ which read `lc`-format catalogs and add size, magnitude, shape etc information consecutively. All the auxiliary files used in the reduction process described here are stored as `lc`-format catalogs for ease of manipulation. Users of our database may find `lc` useful for extracting variables of interest from our catalogs and for applying selection criteria to select sub-catalogs.